J. Fluid Mech. (2017), *vol.* 828, *pp.* 708–732.

doi:10.1017/jfm.2017.494

On the Beltramian motion of the bidirectional vortex in a conical cyclone

Timothy A. Barber[1,‡] **and Joseph Majdalani**[1,†]

[1]Department of Aerospace Engineering, Auburn University, Auburn, AL 36849-5338, USA

(Received 28 January 2017; revised 24 June 2017; accepted 17 July 2017;
first published online 12 September 2017)

In this work, an exact Eulerian model is used to describe the steady-state motion of a bidirectional vortex in a conical chamber. This particular model is applicable to idealized representations of cyclone separators and liquid rocket engines with slowly expanding chamber cross-sections. The corresponding bulk motion is assumed to be non-reactive, rotational, inviscid and incompressible. Then, following Bloor & Ingham (*J. Fluid Mech.*, vol. 178, 1987, pp. 507–519), the spherical Bragg–Hawthorne equation is used to construct a mathematical model that connects the solution to the swirl number and the cone divergence angle. Consequently, a self-similar formulation is obtained independently of the cone's finite body length. This enables us to characterize the problem using closed-form approximations of the principal flow variables. Among the cyclonic parameters of interest, the mantle divergence angle and the maximum cross-flow velocity are obtained explicitly. The mantle consists of a spinning cone that separates the circumferential inflow region from the central outflow. This interfacial layer bisects the fluid domain at approximately 60 per cent of the cone's divergence half-angle. Its accurate determination is proven asymptotically using two different criteria, one being preferred by experimentalists. Finally, recognizing that the flow in question is of the Beltramian type, results are systematically described over a range of cone angles and spatial locations in both spherical and cylindrical coordinates; they are also compared to available experimental and numerical data.

Key words: geophysical and geological flows, rotating flows, vortex flows

1. Introduction

Cyclonic flow field modelling is presently undergoing an era of renewed interest, especially in advanced propulsion-related combustion devices, where swirl-dominated cyclonic motions have proven to be beneficial due to their self-cooling properties, enhanced stability and elevated efficiencies. Several prototypical engines driven by liquid propellant or hybrid fuel combustion are under development today following the bidirectional vortex notion introduced by Knuth and co-workers in 1996. Some

†Email address for correspondence: joe.majdalani@auburn.edu
‡Present address: CSRA Inc., Huntsville, AL 35806, USA.

examples include those concerned with swirl-driven hybrid rocket engines by Knuth *et al.* (1996, 2002) and those associated with liquid–liquid thrust chambers by Sauer *et al.* (2002), Chiaverini *et al.* (2003) and Majdalani (2007, 2012). In this context, a bipolar vortex denotes a cyclone with a pair of outer and inner coaxial, co-rotating swirling streams that are separated by a spinning wheel known as the mantle. The latter constitutes a rotating, non-translating layer along which mass can cross inwardly from the outer, annular vortex to the inner, central core region, where stable combustion and dynamic mixing are sustained.

So far, using cylindrically shaped cyclonic chambers, analytical models have been developed by Vyas & Majdalani (2006) and Majdalani & Rienstra (2007) for the liquid–liquid engine application and by Majdalani (2007) for the hybrid engine configuration. Cold flow experiments using particle image velocimetry (PIV) have been undertaken in parallel by Rom, Anderson & Chiaverini (2004) and Rom (2006). In the same vein, numerical simulations have been carried out under both cold and reactive flow conditions by Fang, Majdalani & Chiaverini (2003) and Majdalani & Chiaverini (2017).

Prior to its use in liquid and hybrid thrust engines, the bidirectional vortex concept was first implemented in industrial cyclones. Being focused on flow filtration rather than propulsion, some of the earliest analyses of cyclonic flow fields may be traced back to experimental and semi-empirical studies of dust separators. In this vein, Shepherd & Lapple (1939, 1940) devised an expansive cyclone separator circuit to study and quantify basic flow characteristics such as velocities, pressures, frictional losses, vortical structures, inlet variations and dust loading impacts on the pressure drop. Along similar lines, Alexander (1949) sought to characterize cyclonic variables with the inclusion of thermal effects. In the same year, ter Linden (1949) investigated the effects of varying the length of the vortex finder on the cyclone separator's efficiency. Then in the spirit of optimization, Stairmand (1951) developed two cyclone designs that either maximized the separator's efficiency or its mass flow rate.

In shifting attention from air to water as the working medium, several pioneering works come to mind, and these date back to Kelsall (1952) and his ultramicroscope illumination method to measure the tangential speed of fine aluminium particulates that are entrained in a hydrocyclone. Kelsall's apparatus consisted of a so-called 'cylinder on cone' made of cast acrylic walls that facilitated the accurate measurement of both tangential and axial flow velocities, hence leaving the radial speed to be deduced from mass conservation. In a follow-up study, Kelsall (1953) reported a body of experimental data that helped to characterize the separation efficiency of hydrocyclones.

Noting the relevance of hydrocyclones to the ore and mining industries, Fontein & Dijksman (1953) sought to characterize the pressure behaviour and tangential velocities in their innovatively designed cyclonic device. By inserting a freely spinning spindle with paddles into the air core, they were able to acquire measurements at various axial elevations.

Sliding on to the mid-decade in Germany, Barth (1956) focused on the characterization of the separation efficiency, which depended on the smallest size particle that could still be separated. To this end, Barth (1956) applied the equilibrium-orbit model or static particle theory, where the balance between centrifugal and particle drag forces determined the motion of an entrained particle. In this manner, he was able to predict the critical particle diameter below which particles would drift inwardly.

Then using a series of experiments by Smith (1962*a*,*b*), the mantle location in a hydrocyclone was measured and catalogued along the length of the separator. It was

found that despite the use of a vortex finder, the axial variation of the mantle location remained small and that two possible locations of the mantle existed, namely, 0.62 and 0.72. A decade later, Leith & Licht (1972) developed an empirical correlation for the collection efficiency of a gaseous cyclone, which could be conveniently used in the design of high efficiency flow separators. In a follow-up study of dust collection devices, Leith & Mehta (1973) reviewed several procedures that existed for estimating the pressure drop and collection efficiency. By evaluating these theories against experimental measurements, they identified the most optimal pressure drop and efficiency theories that could lead to an improved design optimization procedure for cyclone separators.

Returning back to characteristic studies of hydrocyclones, Knowles, Woods & Feuerstein (1973) investigated the three-dimensional flow patterns that evolved in the absence of an air core using tracer particles and cine photography. These researchers compared their results to those observed in hydrocyclones that operated with an air core and found them to be consistent.

Furthermore, by decomposing a cyclone into an inlet, a downflow and an upflow region, Dietz (1981) was able to develop an analytic formulation for the collection efficiency of a reverse-flow cyclone. Also in the spirit of establishing a design optimization procedure, Boysan, Ayers & Swithenbank (1982) resorted to a two-phase algebraic turbulence model of gaseous cyclones with entrained particles to develop a computational tool that could predict grade-efficiency curves based on stochastic particle tracking.

With the advancement of flow visualization techniques, Dabir & Petty (1986) were able to use laser Doppler anemometry in combination with dye injection to confirm that up to four reversals or countercurrent flows could evolve in the conical section of a hydrocyclone with a two-to-one vortex finder contraction. They also confirmed that the mean tangential velocity remained nearly independent of the axial distance, unlike the axial velocity at the centreline, which varied linearly with the elevation. In a similar configuration, Chu & Chen (1993) used a particle dynamics analyser to accurately measure the radial and axial velocities along with the particle sizes and concentrations at various axial stations inside a transparent hydrocyclone.

It should be noted that, in contrast to the critical size efficiency, the collection efficiency is defined as the ratio of the mass flowrate of particles recovered to that of particles introduced into a cyclone separator. In this context, Li, Lin & Vatistas (1987) considered that the incoming momentums of both the carrying medium and the suspended particles remained conserved in a fundamentally frictionless cyclone separator. This enabled them to apply the moment of momentum analysis in conjunction with the stability-radius theory to predict the collection efficiency within approximately 6 per cent of reported values.

Along similar lines, Iozia & Leith (1989) employed the static-particle theory to estimate the maximum tangential velocity and the radius of the forced vortex core which, in turn, could be used to predict cyclone collection efficiencies. According to this particular approach, particles of a critical size would remain suspended at the edge of the forced vortex region where the tangential velocity reached its peak value, namely, at the equilibrium point between particle inertia and viscous drag. This work was later complemented by Xiang, Park & Lee (2001), who investigated the role of the cone's tip dimensions on the separator's collection efficiency. These efforts were also augmented by Avci & Karagoz (2003), who developed analytical models for the collection efficiency and cutoff size as functions of the cyclone's geometric and physical properties. These included the cone's apex diameter, height,

inlet width, surface friction, vortex length and flow regime. Then using a cylindrical swirl tube with inlet vanes, Peng, Hoffmann & Dries (2004) obtained experimental measurements for the overall efficiency, pressure drop and grade-efficiency curves; they also showed that their experimental findings agreed reasonably well with model predictions developed for a tangential inlet, cylinder-on-cone cyclone.

Computationally, in one of the most detailed models developed up to that point, Concha *et al.* (1996) proposed different sets of equations that could be applied to each of the six separate zones that they identified in a hydrocyclone. These equations enabled them to compute the local velocities with a sufficient degree of precision. Then, using the momentum balance of particle trajectories, they were able to deduce the characteristic separation size.

In the context of flow filtration, work on cyclonic dust separators continued to receive attention as documented in several thoroughly detailed articles, especially those involving numerical simulations. For example Hoekstra, Derksen & van den Akker (1999) carried out both experimental and numerical investigations of gaseous, reverse-flow cyclone separators, where three turbulence closure models were tested. In relation to their experimental measurements, these researchers found that the Reynolds stress transport model provided more reasonable predictions than simulations based on the eddy viscosity approach. Their work was further extended by Derksen & van den Akker (2000), who used large eddy simulations to predict the fundamental flow features evolving in a reverse-flow cyclone separator. Their investigation included the precession patterns of the core vortex and its stabilizing role. In a follow-up study, Derksen (2003) conducted large eddy simulations of a high efficiency Stairmand-type cyclone using frozen-field, eddy-lifetime and periodic-flow approaches. Two-phase flow effects on computations were also considered by Derksen, van den Akker & Sundaresan (2008). Conversely, to avert the computational cost entailed in large eddy simulations, Hu *et al.* (2005) modified the empirical constants for anisotropic turbulence to arrive at an improved Reynolds stress model for strongly swirling flows. Their three-dimensional computations were also shown to agree with measurements acquired in a volute separator using laser Doppler velocimetry. This series of studies culminated in a review article by Cortes & Gil (2007), who surveyed various models for inverse-flow cyclone separators and their ability to predict the tangential velocity distribution, pressure drop and collection efficiency.

For the conical cyclone, one the earliest theoretical studies of note may be attributed to Fontein & Dijksman (1953). Therein, semi-empirical approaches are used to construct physically viable approximations of the motion entailed in conically shaped flow separators. A more refined model based on explicit, small-angle expansions (i.e. of the type $\sin\theta \approx \theta$, which are suitable for small cone divergence angles) is later suggested by Bloor & Ingham (1973); these researchers also compare their analytical predictions to experimental measurements by Kelsall (1952). Then after a period of inactivity in this field, the small-angle expansion is superseded by a more realistic approximation for the conical cyclone, which does not make use of the small-angle approximation (Bloor & Ingham 1987). Nonetheless, its resulting solution is still shown to be suitable for small cone angles only. In fact, what we refer to as the Bloor–Ingham model will later prove to substantially outperform its predecessors, especially in its ability to reproduce the overall features of the motion in conical cyclones. For example, despite its inviscid character and limitations to small cone angles and simplistic boundary conditions, the Bloor–Ingham solution is repeatedly shown to exhibit similar characteristics to the flow simulated numerically by Hsieh & Rajamani (1991), Hoekstra *et al.* (1999) and Derksen & van den Akker (2000).

For this reason, the Bloor–Ingham model will be carefully revisited and extended in the context of a conically shaped cyclonic chamber.

Realizing that the conical configuration remains of fundamental relevance to both industrial cyclones and modern contraptions of liquid and hybrid thrust engines, the present study aims at reproducing an exact form of the Bloor–Ingham solution that remains applicable at large divergence half-angles. Using a judicious choice of normalized variables and curvilinear coordinates, our approach will therefore extend the work of Bloor & Ingham (1987). This will be accomplished by using the spherical Bragg–Hawthorne equation as the basis for deriving an exact inviscid solution of the Beltramian type. Not only will the new solution be shown to satisfy Euler's equation identically, it will be further used to unravel essential flow parameters, such as the conical swirl number, cross-flow velocity, pressure, vorticity and mantle locations, in a manner to obviate the need for scaling or conjecture. Finally, the salient flow features in this problem will be discussed and compared whenever possible to existing models in the literature.

2. Problem formulation

2.1. *Geometry*

Our cyclonic separator is idealized as a cone with a divergence half-angle α and length L. The schematic diagram in figure 1 incorporates both the divergent body and the non-divergent cylindrical segment, termed the vortex finder. The present analysis is limited to the divergent segment of this device; the vortex finder plays the equivalent role of an outlet nozzle in a conical thrust chamber. Whether using cylindrical or spherical coordinates, the origin of the reference frame may be anchored at the apex of the cone. Mass addition takes place tangentially, at an average injection speed of U and volumetric flowrate $\bar{Q}_i$. The injected stream then turns axially, leading to a downdraft at an average axial velocity of W (see figure 2). This inwardly directed spiral generates the outer vortex by completely filling the annular region extending from the mantle to the wall. Inside the mantle, an inner vortex is formed through which fluid is carried upwardly and out of the chamber. In this work, we are not concerned with the three-dimensional development of the tangential source into an axial stream. We follow Bloor & Ingham (1987) and assume that the flow turning process is immediate. As for the outer vortex in the exit plane, it remains bounded by the inner and outer radii, b and a. As shown in figure 2(a), we use a right-handed coordinate system consisting of a spherical radius $\bar{R}$, a zenith angle ϕ and an azimuthal angle θ, which is taken to be positive in the direction of swirl.

2.2. *Spherical equations and assumptions*

To start, the flow may be classified as steady, inviscid, incompressible, rotational, axisymmetric and non-reactive. When these assumptions are in place, the conservation of mass and momentum equations become

$$\frac{\partial}{\partial \bar{R}}(\bar{u}_R \bar{R}^2 \sin\phi) + \frac{\partial}{\partial \phi}(\bar{u}_\phi \bar{R} \sin\phi) = 0 \quad \text{(continuity)}, \tag{2.1}$$

$$\bar{u}_R \frac{\partial \bar{u}_R}{\partial \bar{R}} + \frac{\bar{u}_\phi}{\bar{R}} \frac{\partial \bar{u}_R}{\partial \phi} = -\frac{1}{\rho} \frac{\partial \bar{p}}{\partial \bar{R}} \quad \text{(radial)}, \tag{2.2}$$

$$\bar{u}_R \frac{\partial \bar{u}_\phi}{\partial \bar{R}} + \frac{\bar{u}_\phi}{\bar{R}} \frac{\partial \bar{u}_\phi}{\partial \phi} + \frac{\bar{u}_R \bar{u}_\phi}{\bar{R}} - \frac{\bar{u}_\theta^2 \cot\phi}{\bar{R}} = -\frac{1}{\rho \bar{R}} \frac{\partial \bar{p}}{\partial \phi} \quad \text{(zenith)}, \tag{2.3}$$

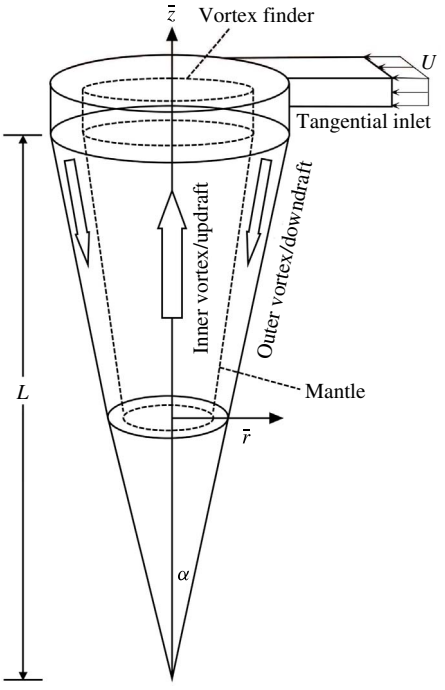

FIGURE 1. Schematic of a conical cyclone separator where the outer and inner vortex regions are clearly depicted.

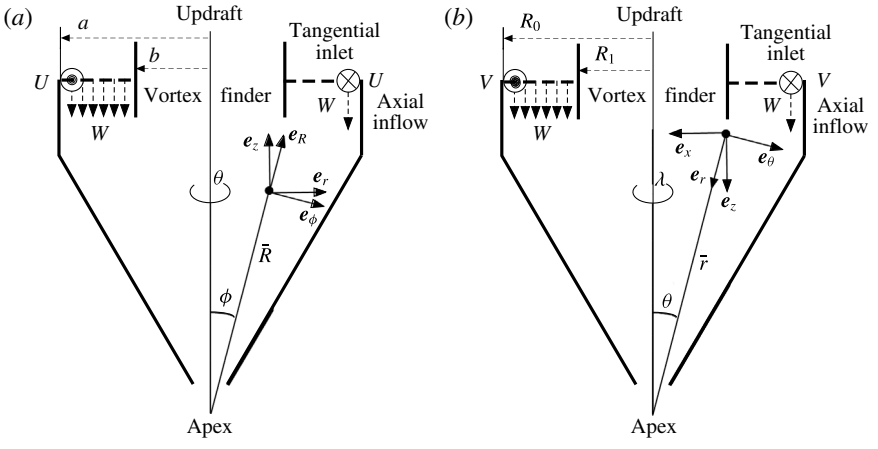

FIGURE 2. Geometric model and coordinate systems adopted by (*a*) the present analysis and (*b*) Bloor & Ingham (1987). Everywhere, an overbar denotes a dimensional quantity. The relabelling in (*a*) leads to the same azimuthal velocity, azimuthal coordinate and polar radius in both spherical and cylindrical coordinates, which are often used in modelling cyclonic flows.

$$\bar{u}_R \frac{\partial \bar{u}_\theta}{\partial \bar{R}} + \frac{\bar{u}_\phi}{\bar{R}} \frac{\partial \bar{u}_\theta}{\partial \phi} + (\bar{u}_R + \bar{u}_\phi \cot \phi) \frac{\bar{u}_\theta}{\bar{R}} = 0 \quad \text{(azimuthal)}, \tag{2.4}$$

with vorticity being expressible by

$$\bar{\boldsymbol{\omega}} = \frac{1}{\bar{R}\sin\phi}\frac{\partial(\bar{u}_\theta \sin\phi)}{\partial\phi}\boldsymbol{e}_R + \frac{1}{\bar{R}}\frac{\partial(\bar{R}\bar{u}_\theta)}{\partial\bar{R}}\boldsymbol{e}_\phi + \frac{1}{\bar{R}}\left[\frac{\partial(\bar{R}\bar{u}_\phi)}{\partial\bar{R}} - \frac{\partial\bar{u}_R}{\partial\phi}\right]\boldsymbol{e}_\theta. \tag{2.5}$$

2.3. *Boundary conditions*

Given axisymmetric motion with respect to the azimuth, our conical flow field can be made to satisfy two conditions on the streamfunction, $\bar{\psi}(\bar{R}, \phi)$. By insisting that $\bar{\psi}$ vanishes both at the centreline and the conical wall (i.e. $\phi = \alpha$), one can take

$$\bar{\psi}(\bar{R}, 0) = \bar{\psi}(\bar{R}, \alpha) = 0. \tag{2.6}$$

Furthermore, one can assume that the tangential inlet is a source by letting $\bar{u}_\theta(\bar{R}_i, \phi_i) = U$. The radius and zenith angle associated with inlet conditions are given by $\bar{R}_i = \sqrt{L^2 + a^2}$ and $\phi_i = \alpha = \tan^{-1}(a/L)$. The same tangential injection is responsible for producing the flow entering the annular section of the outer vortex (i.e. the downdraft in figure 1). Finally, one may verify that mass balance between the outer, annular vortex and the inner, core vortex is strictly maintained. By integrating the solution over the inlet and outlet sections, it may be readily confirmed that $\bar{Q}_o = \bar{Q}_i = UA_i$.

Naturally, the flow injected tangentially along the periphery must turn inwardly. We therefore take W as the average axial velocity at entry, where $b \leqslant \bar{r} \leqslant a$. The streamfunction for a uniform profile enables us to put $\mathrm{d}\bar{\psi}/\mathrm{d}(\bar{R}\sin\phi) = W\bar{R}\sin\phi$, so that

$$\bar{\psi} = \tfrac{1}{2}W(a^2 - \bar{R}^2\sin^2\phi), \tag{2.7}$$

where the choice of integration constants corresponds to a vanishing streamfunction at the wall. The volumetric flow rate at the inlet in terms of the axial velocity becomes

$$\bar{Q}_i = \pi(b^2 - a^2)W. \tag{2.8}$$

2.4. *Normalization*

Compared to the nomenclature used by Majdalani & Rienstra (2007), overbars are removed during the normalization process. This is accomplished by taking

$$R = \frac{\bar{R}}{a};\quad r = \frac{\bar{r}}{a};\quad z = \frac{\bar{z}}{a};\quad l = \frac{L}{a};\quad u_R = \frac{\bar{u}_R}{U};\quad u_\phi = \frac{\bar{u}_\phi}{U};\quad u_\theta = \frac{\bar{u}_\theta}{U}, \tag{2.9a–g}$$

$$B = \frac{\bar{B}}{Ua};\quad H = \frac{\bar{H}}{U^2};\quad p = \frac{\bar{p}}{\rho U^2};\quad \psi = \frac{\bar{\psi}}{Ua^2};\quad Q_i = \frac{\bar{Q}_i}{Ua^2};\quad \sigma_c = \frac{a^2 - b^2}{A_i}, \tag{2.10a–f}$$

where the conical swirl number, σ_c, is described in appendix A. In the above, B, H and p represent the angular momentum, stagnation head and pressure, respectively. In addition, we find it useful to associate the cylindrical radii r_ϕ and r_α with the zenith angles ϕ and α, where r_α denotes the horizontal distance from the cone axis to the inclined wall. This enables us to define the horizontal radial fraction in any axial plane using

$$X_\phi = \frac{r_\phi}{r_\alpha} = \frac{\tan\phi}{\tan\alpha}. \tag{2.11}$$

Accordingly, the locally normalized radial distance corresponding to the open outflow fraction may be expressed as $X_\beta = r_\beta/r_\alpha = b/a$ at any axial elevation z. Furthermore, owing to the geometric similarity at fixed divergence angle, the length L does not appear in a judiciously normalized system, where it may be readily supplanted by $l = \cot\alpha$.

3. Solution

3.1. *Bragg–Hawthorne equation*

Euler's equation can be written as $\nabla H - \boldsymbol{u} \times \boldsymbol{\omega} = 0$, where $H = p + u^2/2$ represents the dimensionless fluid head. For a given streamfunction, $\psi(R, \phi)$, the radial and zenith velocities may be expressed as

$$u_R = \frac{1}{R^2 \sin\phi} \frac{\partial \psi}{\partial \phi}; \quad u_\phi = -\frac{1}{R \sin\phi} \frac{\partial \psi}{\partial R}. \tag{3.1a,b}$$

Based on the θ-momentum equation, we group $u_\theta R \sin\phi$ and convert (2.4) into

$$u_R \frac{\partial}{\partial R}(u_\theta R \sin\phi) + \frac{u_\phi}{R} \frac{\partial}{\partial \phi}(u_\theta R \sin\phi) = 0. \tag{3.2}$$

The resulting material derivative directly leads to the tangential velocity,

$$u_\theta R \sin\phi = B(\psi) \quad \text{or} \quad u_\theta = \frac{B(\psi)}{R \sin\phi}, \tag{3.3a,b}$$

where the tangential angular momentum, $B(\psi)$, is yet to be determined. Using the free vortex relation for the tangential velocity, $B(\psi)$ may be linked to the radial vorticity, ω_R. By substituting u_θ into (2.5), we retrieve

$$\omega_R = \frac{1}{R^2 \sin\phi} \frac{\mathrm{d}B}{\mathrm{d}\psi} \frac{\partial \psi}{\partial \phi}, \tag{3.4}$$

where the derivative with respect to ψ is used in view of $B = B(\psi)$. Next, the tangential vorticity may be extracted from the ϕ-momentum equation. Transforming $\nabla H - \boldsymbol{u} \times \boldsymbol{\omega} = 0$ into scalar form, we segregate the ϕ-component and write

$$\frac{1}{R} \frac{\mathrm{d}H}{\mathrm{d}\psi} \frac{\partial \psi}{\partial \phi} + \frac{1}{R^2 \sin\phi} \omega_\theta - \frac{B(\psi)}{R \sin\phi} \left(\frac{1}{R^2 \sin\phi} \frac{\mathrm{d}B}{\mathrm{d}\psi} \frac{\partial \psi}{\partial \phi} \right) = 0. \tag{3.5}$$

This expression may be considerably simplified and rearranged into

$$\frac{\omega_\theta}{R \sin\phi} = \frac{1}{R^2 \sin^2\phi} B(\psi) \frac{\mathrm{d}B}{\mathrm{d}\psi} - \frac{\mathrm{d}H}{\mathrm{d}\psi}. \tag{3.6}$$

After inserting ω_θ from (2.5) into (3.6), the velocities may be eliminated through (3.1). The outcome is a form of the Bragg–Hawthorne equation in spherical coordinates, namely,

$$\frac{\partial^2 \psi}{\partial R^2} + \frac{\sin\phi}{R^2} \frac{\partial}{\partial \phi} \left(\frac{1}{\sin\phi} \frac{\partial \psi}{\partial \phi} \right) = R^2 \sin^2\phi \frac{\mathrm{d}H}{\mathrm{d}\psi} - B(\psi) \frac{\mathrm{d}B}{\mathrm{d}\psi}. \tag{3.7}$$

In what follows, the proper choice of $B(\psi)$ and $H(\psi)$ will be instrumental to the solution of (3.7). In order to link B and H, we consider the inlet condition where the tangential velocity enters at an average velocity of U. Based on the tangential momentum equation, we have

$$u_\theta R \sin\phi = B(\psi), \tag{3.8}$$

where B remains constant along a streamline. Next we differentiate (2.7) and (3.8) with respect to $R\sin\phi$ to obtain, at the top section of the cone,

$$\frac{\mathrm{d}B}{\mathrm{d}(R\sin\phi)} = 1; \quad \frac{\mathrm{d}\psi}{\mathrm{d}(R\sin\phi)} = \frac{R\sin\phi}{\pi\sigma_c}. \tag{3.9a,b}$$

A combination of these two expressions leads to

$$B\frac{\mathrm{d}B}{\mathrm{d}\psi} = \pi\sigma_c \equiv \kappa_c = \text{const.} \tag{3.10}$$

This relation grants the tangential velocity the freedom to vary with the streamfunction. Assuming a constant inlet velocity, we have $\mathrm{d}H/\mathrm{d}\psi = 0$. Furthermore, in view of the flow being isentropic, the total enthalpy variation reduces to that of the stagnation pressure head (Bragg & Hawthorne 1950). These substitutions into the Bragg–Hawthorne equation lead to a substantially more compact form, namely,

$$\frac{\partial^2\psi}{\partial R^2} + \frac{\sin\phi}{R^2}\frac{\partial}{\partial\phi}\left(\frac{1}{\sin\phi}\frac{\partial\psi}{\partial\phi}\right) = -\kappa_c. \tag{3.11}$$

3.2. *Streamfunction and velocities*

In seeking an exact solution, we posit $\psi = R^2G(\phi)$ and, pursuant to the work detailed in § B.1, we obtain

$$\psi = \tfrac{1}{2}\kappa_c R^2\sin^2\phi(\lambda - \ln\Phi + \csc\phi\cot\phi - \csc^2\phi), \tag{3.12}$$

where

$$\lambda = \csc^2\alpha - \csc\alpha\cot\alpha + \ln\Phi_\alpha = \Phi_\alpha\csc\alpha + \ln\Phi_\alpha \tag{3.13}$$

$$\Phi \equiv \tan(\tfrac{1}{2}\phi); \quad \Phi_\alpha \equiv \tan(\tfrac{1}{2}\alpha). \tag{3.14a,b}$$

The corresponding velocities become

$$u_R = \kappa_c[(\lambda - \ln\Phi)\cos\phi - 1], \tag{3.15}$$

$$u_\phi = \kappa_c[(\ln\Phi - \lambda)\sin\phi + \Phi] \tag{3.16}$$

and

$$u_\theta = \frac{1}{R\sin\phi}[1 + (\kappa_c R\sin\phi)^2(\lambda - \ln\Phi - \Phi\csc\phi)]^{1/2}. \tag{3.17}$$

Compared to the inviscid model of Vyas & Majdalani (2006), the tangential velocity obtained using this approach retains the free vortex form and, as such, the inverse variation with the distance from the axis of rotation $\sim(R\sin\phi)^{-1}$. Additionally, (3.17) exhibits a crucial dependence on the inlet velocity profile and the spatially varying streamfunction. It can therefore be seen that the characteristic features of this procedure consist of, first, retaining the spatial dependence granted by the streamfunction and, second, accounting for a specific axial injection profile at entry.

At this stage, using the subscript 'BI' to denote the model by Bloor & Ingham (1987), one may write

$$\psi_{BI} = \tfrac{1}{2}\kappa_c R^2\sin^2\phi[\lambda_{BI} - \ln(\tfrac{1}{2}\tan\phi) + \csc\phi\cot\phi - \csc^2\phi], \tag{3.18}$$

where $\lambda_{BI} \equiv \csc^2\alpha - \cot\alpha\csc\alpha + \ln[(\tan\alpha)/2]$. Note that for small cone angles, (3.18) may be recovered asymptotically from (3.12) using successively imposed small-angle approximations, $\tan(\phi/2) \approx \phi/2 \approx (\tan\phi)/2$. Although the dual displacement of the $1/2$ in the streamfunction may seem negligible at first, it can be shown to have a significant impact on the subsequent flow properties, especially for large cone angles.

3.3. *Equivalent cylindrical polar values*

In the interest of clarity, our expressions are transformed into their polar cylindrical equivalents. The switch between spherical and cylindrical coordinates follows the standard transformation matrix (§ B.3). By substituting the values for the radial and zenith velocities, the radial and axial velocities in a cylindrical reference frame emerge. Thus, the streamfunction and velocities may be collapsed into

$$u_r = -\kappa_c \Phi; \quad u_z = \kappa_c(\lambda - \ln \Phi - 1). \tag{3.19a,b}$$

To convert the streamfunction and velocities into cylindrical coordinates, we employ $R = \sqrt{r^2 + z^2}$, $\sin\phi = r/R$, $\cos\phi = z/R$, and $\phi = \tan^{-1}(r/z)$. These relations yield

$$\psi = \tfrac{1}{2}\kappa_c r^2 \left(\lambda - \ln Z - Z\sqrt{1+\zeta^2}\right), \tag{3.20}$$

$$u_R = \kappa_c[\zeta(\lambda - \ln Z)(1+\zeta^2)^{-1/2} - 1], \tag{3.21}$$

$$u_\phi = -\kappa_c[(\lambda - \ln Z)(1+\zeta^2)^{-1/2} - Z], \tag{3.22}$$

$$u_\theta = \frac{1}{r}\left[1 + (r\kappa_c)^2\left(\lambda - \ln Z - Z\sqrt{1+\zeta^2}\right)\right]^{1/2} \tag{3.23}$$

and

$$u_r = -\kappa_c Z; \quad u_z = \kappa_c(\lambda - \ln Z - 1), \tag{3.24a,b}$$

where the dimensionless variables ζ and Z stand for z/r and $\sqrt{1+\zeta^2} - \zeta$, respectively.

4. Results and discussion

4.1. *Mantle locations*

One of the earliest mentions of the term 'mantle' in connection with cyclone separators dates back to Bradley and Pulling (1959; 1965). In this context, Bradley (1965) defines the mantle as the locus of zero vertical velocity. This locus is specified by the angle at which either u_R or u_z vanishes. Consequently, two mantle inclinations may be defined in a conical chamber as a function of the zenith angle ϕ. The first, β_R, corresponds to the location where u_R vanishes, and the second coincides with the angle, β_z, where $u_z = 0$. These can be obtained sequentially from

$$\left.\begin{aligned} u_R = 0 : \left\{\lambda - \ln\left[\tan\left(\tfrac{1}{2}\beta_R\right)\right]\right\}\cos\beta_R - 1 = 0, \\ u_z = 0 : \lambda - \ln\left[\tan\left(\tfrac{1}{2}\beta_z\right)\right] - 1 = 0. \end{aligned}\right\} \tag{4.1}$$

In order to determine the mantle location asymptotically, we first consider the behaviour of the radial velocity u_R and its corresponding cylindrical velocity, u_z, as these components direct the flow into and out of the cyclonic chamber. In theory, the two mantles are located where $u_R = 0$ and $u_z = 0$, respectively, thus defining two conical surfaces along which the flow switches polarity between a downward and an upward spiral. Similar experimental and numerical patterns are reported by Pervov (1974), Luo *et al.* (1989), Zhou & Soo (1990), Peng *et al.* (2002) and Hu *et al.* (2005). Because u_R or u_z appear as functions of the zenith angle ϕ, we solve for the root of $u_R = 0$ and $u_z = 0$, and call these inclination angles β_R and β_z, respectively. Based on (4.1), we set $1 - \lambda\cos\beta_R + \ln\Phi_{\beta_R}\cos\beta_R = 0$ and $1 - \lambda + \ln\Phi_{\beta_z} = 0$, where

$\Phi_{\beta_R} = \tan(\beta_R/2)$ and $\Phi_{\beta_z} = \tan(\beta_z/2)$. We then use a MacLaurin series expansion to extract

$$\left.\begin{array}{c} u_R = 0 : 1 - \lambda + \ln\left(\frac{1}{2}\beta_R\right) + \left(\frac{1}{2}\beta_R\right)^2\left(\frac{1}{3} + 2\lambda + 2\ln 2\right) + \cdots = 0, \\ u_z = 0 : 1 - \lambda + \ln\left(\frac{1}{2}\beta_z\right) + \frac{1}{12}\beta_z^2 + \cdots = 0. \end{array}\right\} \tag{4.2}$$

In actuality, of the twelve algebraic roots that emerge for β_R, only two are meaningful, namely,

$$\tilde{\beta}_R = \begin{cases} \dfrac{\sqrt{-\mathrm{pln}[4(\lambda + \ln 2 + \frac{1}{6})\mathrm{e}^{2(\lambda-1)}]}}{\sqrt{\lambda + \ln 2 + \frac{1}{6}}}, & 0 < \alpha \leqslant \alpha_0, \\ \dfrac{\sqrt{\mathrm{pln}[4(\lambda + \ln 2 + \frac{1}{6})\mathrm{e}^{2(\lambda-1)}]}}{\sqrt{\lambda + \ln 2 + \frac{1}{6}}}, & \alpha_0 < \alpha < \dfrac{1}{2}\pi, \end{cases} \tag{4.3}$$

where $\alpha_0 = 0.48785(27.952^\circ)$, with the tilde denoting an asymptotic approximation. Fortuitously, it may be shown that the piecewise representation in (4.3) may be collapsed into a single, uniformly valid expression for the mantle location, namely,

$$\tilde{\beta}_R = \sqrt{\frac{\mathrm{pln}[4(\lambda + \ln 2 + \frac{1}{6})\mathrm{e}^{2(\lambda-1)}]}{\lambda + \ln 2 + \frac{1}{6}}} = \frac{\alpha}{\sqrt{\mathrm{e}}} - \left(\frac{1}{3} - \frac{5}{24}\mathrm{e} + \frac{1}{2}\ln\alpha\right)\left(\frac{\alpha}{\sqrt{\mathrm{e}}}\right)^3 + O(\alpha^5 \ln\alpha) \tag{4.4}$$

and so, using a superscript to denote the asymptotic expansion order, we have

$$\tilde{\beta}_R^{(2)} \approx 0.606531\alpha + 0.0519838\alpha^3 - 0.111565\alpha^3 \ln\alpha. \tag{4.5}$$

By repeating this process for $\beta_z = 2\arctan[\exp(\lambda - 1)]$, twelve algebraic roots may be retrieved, but of these only one proves to be physical, specifically,

$$\tilde{\beta}_z = \sqrt{6\,\mathrm{pln}[\tfrac{2}{3}\mathrm{e}^{2(\lambda-1)}]} = \frac{\alpha}{\sqrt{\mathrm{e}}} + \frac{5\mathrm{e} - 2}{24}\left(\frac{\alpha}{\sqrt{\mathrm{e}}}\right)^3 + \frac{100 - 300\mathrm{e} + 273\mathrm{e}^2}{5760}\left(\frac{\alpha}{\sqrt{\mathrm{e}}}\right)^5 + O(\alpha^7) \tag{4.6}$$

and so

$$\tilde{\beta}_z^{(2)} \approx 0.606531\alpha + 0.107766\alpha^3 + 0.0185508\alpha^5. \tag{4.7}$$

A comparison between (4.5) and (4.7) reinforces the intrinsic similarity between the asymptotic forms of $\tilde{\beta}_z^{(2)}$ and $\tilde{\beta}_R^{(2)}$, which may be traced back to their basic definitions. Alternatively, instead of using the inclination angle β to define the mantle, one may track the mantle vertically using the fraction of the radius X_{β_R} or X_{β_z} corresponding to either $u_R = 0$ or $u_z = 0$. As per (2.11), these are given by

$$X_{\beta_R} = \tan\beta_R / \tan\alpha; \quad X_{\beta_z} = \tan\beta_z / \tan\alpha, \tag{4.8a,b}$$

which can be approximated using

$$\tilde{X}_{\beta_R} = \cot\alpha \tan\left\{\frac{1 + \cos\alpha\,\mathrm{pln}[4\Phi_\alpha^2 \mathrm{e}^{\Phi_\alpha^2 - 1}(\frac{1}{6} + \ln 2\Phi_\alpha + \Phi_\alpha \csc\alpha)]}{1 + (1 + \cos\alpha)[\frac{1}{6} + \ln 2\Phi_\alpha]}\right\}^{1/2} \tag{4.9}$$

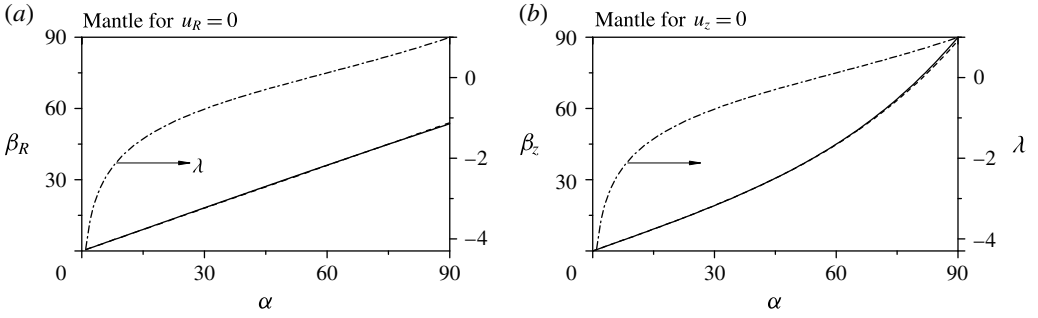

FIGURE 3. Mantle inclination angle versus α as predicted by either (*a*) β_R (——) and $\tilde{\beta}_R^{(0)}$ (– – –) or (*b*) β_z (——) and $\tilde{\beta}_z^{(2)}$ (– – –). Also shown is the connection between these solutions and λ (— · —).

and

$$\tilde{X}_{\beta_z} = \cot\alpha \tan\left[6\sqrt{\mathrm{pln}\left(\tfrac{2}{3}\Phi_\alpha^2 \mathrm{e}^{\Phi_\alpha^2-1}\right)}\right]. \tag{4.10}$$

In practice, a three-term asymptotic expansion for each of the radial fractions may be conveniently retrieved, specifically,

$$\tilde{X}_{\beta_R}^{(2)} = \frac{1}{\sqrt{\mathrm{e}}} - \frac{\mathrm{e}+4\ln\alpha}{8\mathrm{e}\sqrt{\mathrm{e}}}\alpha^2 \approx 0.606531 - 0.0758163\alpha^2 - 0.111565\alpha^2\ln\alpha \tag{4.11}$$

and

$$\begin{aligned}\tilde{X}_{\beta_z}^{(2)} &= \frac{1}{\sqrt{\mathrm{e}}} + \frac{2-\mathrm{e}}{8\mathrm{e}\sqrt{\mathrm{e}}}\alpha^2 + \frac{388+420\mathrm{e}-255\mathrm{e}^2}{5760\mathrm{e}^2\sqrt{\mathrm{e}}}\alpha^4 \\ &\approx 0.606531 - 0.0200338\alpha^2 - 0.00505237\alpha^4.\end{aligned} \tag{4.12}$$

Equations (4.4) and (4.6) are quite illuminating. In view of the small size of $\alpha\mathrm{e}^{-1/2}$, a one-term approximation of the mantle location yields $\beta_R = \beta_z \approx 0.6065\alpha$, which explains the ubiquitous use of $\beta_z = 0.6\alpha$, or alternatively, $X_{\beta_z} = 0.6$, in several empirical studies of conically shaped cyclone separators. Therein, using $u_z = 0$ to define the mantle seems to be preferred, at least from an experimental perspective, over the $u_R = 0$ criterion. This is owed in large part to the ease with which the $u_z = 0$ condition may be implemented experimentally, or recreated numerically. According to (4.4), the use of $\beta_R = 0.6\alpha$ entails an absolute error that varies between 0.0066 and 0.11° for $1 \leqslant \alpha \leqslant 60°$. In practice, the 60 % mantle inclination is repeatedly reported in several independent investigations, including those by Bradley & Pulling (1959), Pervov (1974), Dabir & Petty (1986), Hoekstra *et al.* (1999) and Chesnokov, Bauman & Flisyuk (2006).

To further characterize the mantle inclination, the functional dependence of β_R and β_z on α is illustrated in figure 3 as well as table 1. Note that λ varies between -4.24 and 1 for $1 \leqslant \alpha \leqslant 90°$. As for the mantle location, both exact and approximate representations are overlaid and shown to be graphically indiscernible, except when the divergence half-angle approaches the impractical value of 90°. Nonetheless, the error incurred in using $\beta_R = 0.6\alpha$ to estimate the mantle location reaches a maximum of 0.44° at $\alpha = 90°$, unlike the error in β_z, which exceeds 1.3° using $\tilde{\beta}_z^{(2)}$. Instead, the

$u_z = 0$ condition leads to a rather uniform ratio X_{β_z} at any axial station. We conclude that, for divergence half-angles below 38°, both β_R and β_z may be suitably relied on to characterize the mantle, as their predictions in this range fall within 5 % or less. For larger angles, only β_R continues to follow the 60 % of α approximation. These results are clearly reflected in table 1.

4.2. *Streamlines*

The streamlines prescribed by (3.20) are shown in figure 4 at four different cone half-angles of 30°, 45°, 60° and 75°. The contour curves represent lines of constant ψ, which illustrate the downdraft, bending and updraft regions. Also shown are the mantle inclinations corresponding to $u_R = 0$ and denoted by β_R. The observed subdivisions of the flow field are consistent with several experimental studies, including those by Shepherd & Lapple (1939), Stairmand (1951), Kelsall (1952), Escudier (1987) and Peng *et al.* (2002). Here the dashed lines represent ψ_{BI}, which clearly deviates from the present solution as α is increased. Interestingly, these streamlines appear as though they are entering the conical chamber through the outlet, instead of the inlet, because the small-angle approximation that the Bloor–Ingham solution is based on deteriorates as ϕ is increased. Furthermore, the differences in streamline curvatures translate into deviations in the velocity components. For example, the relative difference between the exact value of u_R and its predicted value based on ψ_{BI} reaches 5 per cent for a cone half-angle of 28°.

4.3. *Spherical radial and zenith velocity distributions*

The spherical radial velocity, u_R, controls the spherical polarity of the flow. Simply put, negative values imply downward motion along the R coordinate whereas positive values correspond to an updraft (figure 1). In figure 4, the direction and location of the flow are specified. The outer vortex is delineated by the region in which $u_R < 0$, wherein the fluid is transported downwardly in a spiralling fashion. In contrast, the positive u_R region within the inner vortex induces convection of the spinning fluid upwardly and out of the top.

Another feature that may be inferred from u_R concerns the physicality and behaviour of the spherical radial mantle. This corresponds to the surface of revolution where $u_R = 0$. The ensuing mantle inclination remains constant throughout the cone, and this property leads to a constantly changing horizontal location as the axial position is vertically increased. This particular axial shifting is confirmed through (3.21) and may be observed in figure 5, where u_R is plotted at either (*a*) four axial locations or (*b*) five half-angles, to clearly demarcate the inner and outer vortex regions.

By inspection of (3.22), u_ϕ is seen to be solely dependent on the zenith angle and the conical swirl number. Being somewhat akin to the radial velocity of the bidirectional vortex considered by Vyas & Majdalani (2006), u_ϕ vanishes at both the core and the side wall. Conversely at $\phi = \beta_R$ or β_z, the two complementary velocities u_R and u_r provide the necessary link between the inner and outer vortex regions, by permitting mass transport across the mantle interface. Because $u_R = 0$ at $\phi = \beta_R$, the connection across the mantle strictly depends on u_ϕ. As shown in figure 5, the curves exhibit similar profiles where the variation of u_ϕ is shown at four axial cross-sections and five half-angles, respectively. Everywhere between the axis and the wall, u_ϕ retains a negative value that is indicative of inward flow towards the cone axis.

It should be remarked that, in the absence of friction, the forced vortex region that characterizes typical cyclonic cores cannot be fully established. Without properly

https://doi.org/10.1017/jfm.2017.494 Published online by Cambridge University Press

α $\angle$	λ (3.13)	β_R $\angle$	$\tilde{\beta}_R^{(0)}$ $\angle$	β_z $\angle$	$\tilde{\beta}_z^{(2)}$ $\angle$	X_{β_R} (4.8)	$\tilde{X}_{\beta_R}^{(2)}$ (4.11)	X_{β_z} (4.8)	$\tilde{X}_{\beta_z}^{(2)}$ (4.12)	β_R/α %	β_z/α %	$\lvert\beta_R-\beta_z\rvert$ %	$\lvert X_{\beta_R}-X_{\beta_z}\rvert$ %
5°	−2.63	3.0°	3.0°	3.0°	3.0°	0.606	0.608	0.606	0.607	60.7	60.7	0.0	0.0
10°	−1.92	6.1°	6.1°	6.1°	6.1°	0.602	0.610	0.606	0.606	60.6	61.0	0.4	0.4
15°	−1.52	9.1°	9.1°	9.2°	9.2°	0.597	0.612	0.605	0.605	60.6	61.4	0.8	0.8
20°	1.22	12.1°	12.1°	12.6°	12.4°	0.590	0.612	0.604	0.604	60.6	62.0	1.4	1.4
25°	−0.982	15.2°	15.2°	15.7°	15.7°	0.58	0.610	0.603	0.602	60.6	62.8	2.2	2.3
30°	−0.781	18.2°	18.2°	19.1°	19.1°	0.568	0.606	0.601	0.601	60.5	63.8	3.3	3.3
35°	−0.605	21.2°	21.2°	22.7°	22.7°	0.553	0.599	0.598	0.598	60.5	64.9	4.4	4.5
40°	−0.445	24.2°	24.3°	26.5°	26.6°	0.535	0.589	0.595	0.595	60.5	66.4	5.9	6.0
45°	−0.296	27.2°	27.3°	30.6°	30.6°	0.514	0.576	0.592	0.592	60.4	68.0	7.6	7.8
50°	−0.154	30.2°	30.3°	35.0°	35.0°	0.488	0.500	0.588	0.588	60.3	70.0	9.7	10.0
55°	−0.017	33.2°	33.4°	39.8°	39.7°	0.457	0.541	0.582	0.584	60.3	72.3	12.0	12.5
60°	0.117	36.1°	36.4°	45.0°	44.8°	0.421	0.518	0.577	0.578	60.2	74.9	14.7	15.5
65°	0.252	39.1°	49.4°	50.7°	50.4°	0.379	0.491	0.569	0.572	60.1	77.9	17.8	19.0
70°	0.389	42.0°	42.5°	57.0°	56.6°	0.328	0.46	0.560	0.565	60.0	81.4	21.4	23.2
75°	0.530	44.9°	45.5°	67.0°	63.4°	0.267	0.425	0.549	0.557	59.9	85.3	25.4	28.2
80°	0.677	47.8°	48.5°	71.8°	71.0°	0.195	0.386	0.536	0.548	59.8	89.7	29.9	33.9
85°	0.832	50.7°	51.6°	80.4°	79.4°	0.107	0.343	0.520	0.538	59.7	94.6	34.9	41.3
90°	1.000	53.6°	54.6°	90.0°	88.7°	0.000	0.295	1.000	0.526	59.5	100	40.5	100.0

TABLE 1. Properties of the two characteristic mantles at different conical half-angles.

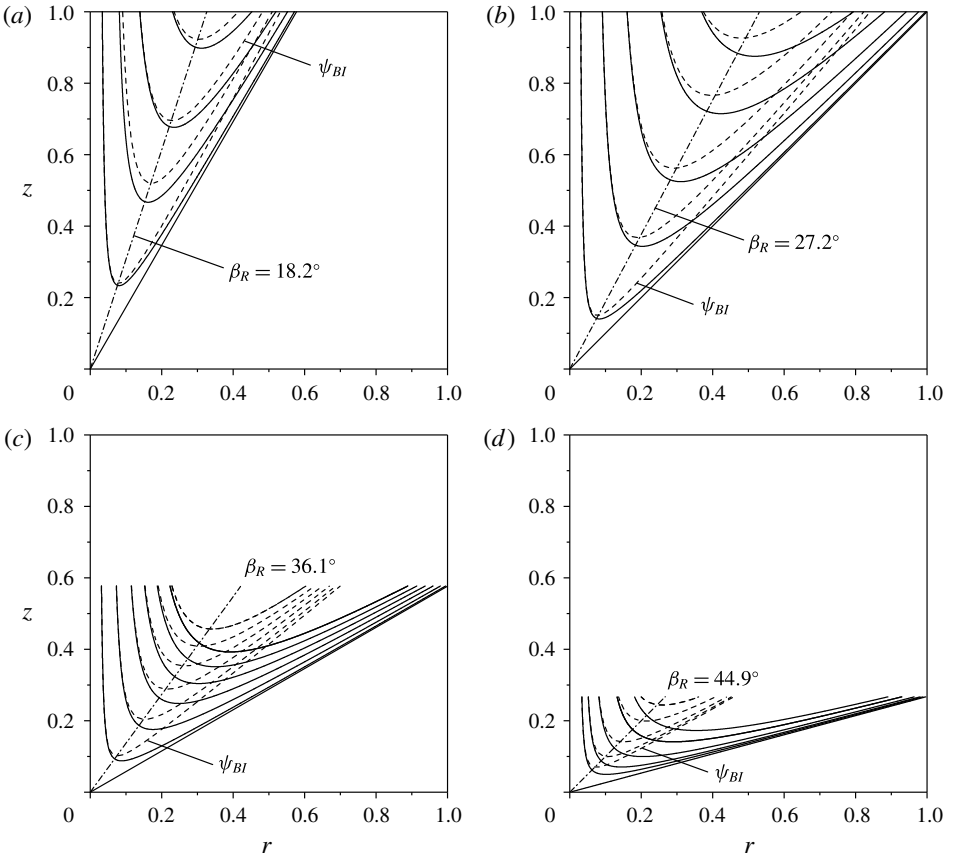

FIGURE 4. Flow streamlines for $\sigma_c = 1$ and cone half-angles of (*a*) 30°, (*b*) 45°, (*c*) 60° and (*d*) 75°. Here, the present model (——) is compared to the small-angle approximation by Bloor & Ingham (1987) (– – –). Also shown are the corresponding mantle inclinations (— · —) of $\beta_R \approx 18°$, 27°, 36° and 45°, respectively.

accounting for shearing stresses in the core region, u_R (and hence u_z) becomes unbounded as $(\phi, r) \to 0$. In a viscous medium, a core boundary layer develops around the centreline to the extent of mitigating any divergence in the velocity. One also expects a thin boundary layer to form along the conical wall, in fulfilment of the no slip requirement.

4.4. *Tangential and axial velocities*

Figure 6 illustrates the behaviour of the swirl and axial velocities compared to the experimental and numerical measurements of Hsieh & Rajamani (1988) and Monredon, Hsieh & Rajamani (1992). We begin with figure 6(*a*,*b*), where the swirl velocity in a polar plane is showcased against available experimental and numerical data at two tangential injection velocities. Also shown on the graphs is the free vortex motion given by $u_\theta = r^{-1}$. The dimensions of the cyclonic contraptions used by Hsieh & Rajamani (1988) and Monredon *et al.* (1992) are so analogous that they yield similar values of the modified swirl number σ_c ($\alpha = 10°$, $a = 0.0375$ m, and $X_{\beta_R} \approx 0.6$). Overall discrepancies observed between theory and measurements or

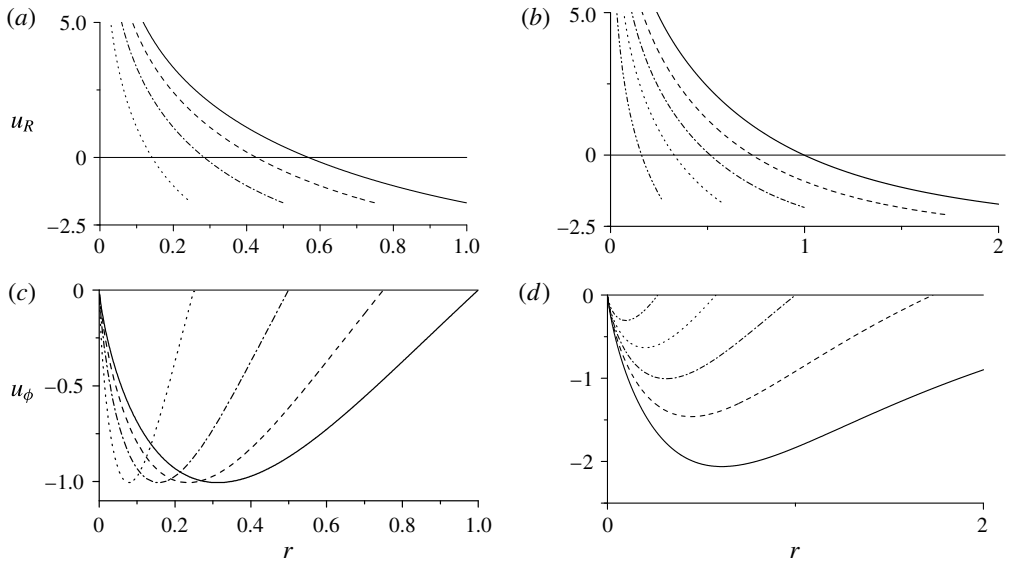

FIGURE 5. Radial and zenith velocity distributions for $\sigma_c = 1$ taken at (*a*,*c*) several axial positions for a fixed divergence half-angle of 45° and (*b*,*d*) several half-angles at the top of the cone where $z/l = 1$. The four curves in (*a*,*c*) correspond to $z/l = 1$ (——), 0.75 (– – –), 0.5 (— · —) and 0.25 (· · · ·). The five curves in (*b*,*d*) correspond to half-angles of $\alpha = 75°$ (——), 60° (– – –), 45° (— · —), 30° (· · · · · ·) and 15° (— · · —).

simulations may be attributed in part to the fundamental limitations of an inviscid model. Consistently with the free vortex form of (3.23), u_θ becomes unbounded as $r \to 0$, and diminishes with the inverse distance from the cone axis. Its axial variation, however, seems to be less pronounced due to its weaker dependence on the streamfunction and the inlet profile. This grants the motion added sensitivity to the inlet conditions, especially when compared to the free vortex model of Vyas & Majdalani (2006). Therein, $u_\theta = r^{-1}$ is solely dependent on the average inlet velocity. In both models, the strictly inviscid form grows to unbounded levels at the core. By the same token, it fails to accommodate the velocity adherence requirement that must be secured at the wall. This result is actually characteristic of most swirl-dominated frictionless flows; it is ascertained in work by Bloor & Ingham (1987), Harvey (1962) and Leibovich (1978, 1984). Interestingly, the axial velocities in figure 6(*c*,*d*) exhibit similar features to those of u_R. These are illustrated for $\sigma_c = 0.2$ and 0.305, respectively. Depending on the vertical distance from the apex, u_z crosses the oblique mantle while switching polarity. A similar transition is observed experimentally by Mothes & Löffler (1985) in their investigation of particle deposition in gaseous cyclones. The agreement between theory and either laboratory measurements or numerical simulations may be viewed as confirmatory, especially when sufficiently removed from the core or the bounding wall.

4.5. *Maximum zenith and cross-flow velocities*

In the vicinity of the mantle, a maximum value of $|u_\phi|$ may be extrapolated. Interestingly, the maximum radial velocity of the bidirectional vortex in a cylinder also occurs in close proximity of the mantle. Here, the maximum $|u_\phi|$ appears at a constant

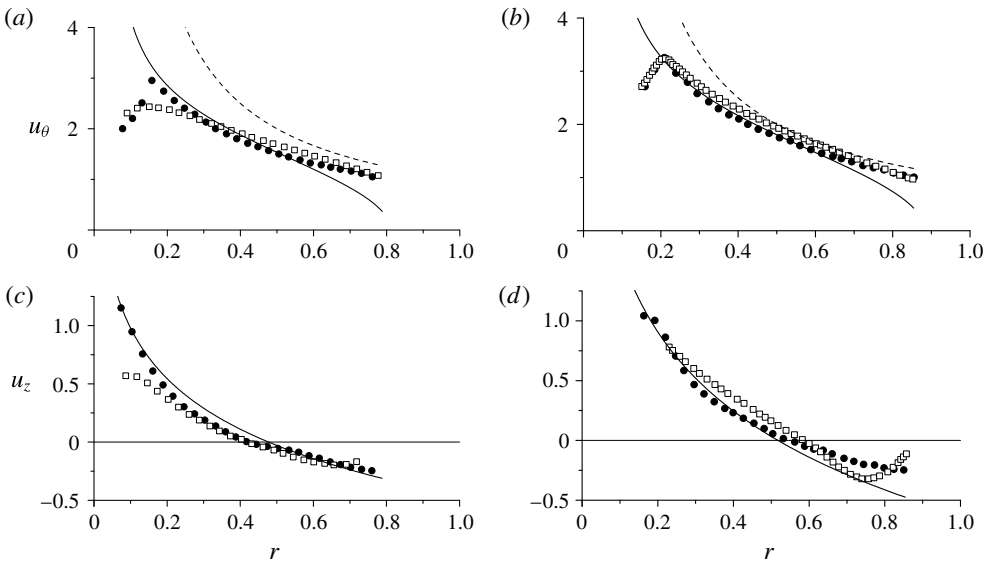

FIGURE 6. Theoretical velocity (——) and the free vortex model (– – –) compared to experimental (●) and numerical (□) data by (*a*,*c*) Hsieh & Rajamani (1988), and (*b*,*d*) Monredon *et al.* (1992). Here we show u_θ for (*a*) $U = 7.98$ m s^{-1} and (*b*) 6.26 m s^{-1}; and u_z for (*c*) $\sigma_c = 0.2$ and (*d*) 0.305.

angle, especially that (3.16) consists of a sole function of ϕ. This angle may be calculated from the derivative with respect to ϕ, namely, $[\sin\phi(\ln\Phi - \lambda) + \Phi]|_{\phi_{max}} = 0$, and so

$$\cos(\phi_{max})(\ln\Phi - \lambda) + \tfrac{1}{2}\sec^2(\tfrac{1}{2}\phi_{max}) + 1 = 0. \tag{4.13}$$

Hence, for every α there exists a corresponding ϕ_{max} that can be evaluated numerically. A practically equivalent analytical root can be deduced in piecewise fashion using

$$\tilde{\phi}_{max} = \begin{cases} 2\sqrt{\mathrm{pln}[-\exp(2\lambda - 3)\vartheta]/\vartheta}; & 0 < \alpha \leqslant \alpha_0;\ \alpha_0 = 0.38732(22.192^\circ), \\ 2\sqrt{\mathrm{pln}[\exp(2\lambda - 3)\vartheta]/\vartheta}; & \alpha_0 < \alpha \leqslant \tfrac{1}{2}\pi, \end{cases} \tag{4.14}$$

where $\vartheta \equiv 3/5 + 4\lambda + 4\ln 2$. In lieu of (4.14), a simple asymptotic approximation for ϕ_{max} may be extracted in degrees and written as

$$\tilde{\phi}_{max}[\mathrm{deg}] \approx 0.3376 + 0.3250\alpha + 0.001185\alpha^2[\mathrm{deg}]; \quad \alpha \geqslant 10^\circ. \tag{4.15}$$

As for the cross-flow velocity, it coincides with the mantle location and may be readily obtained through the simple substitution of $\phi = \beta_R$. We get

$$\begin{aligned} (u_\phi)_{cross} &= \kappa_c[\sin\beta_R(\ln\Phi_{\beta_R} - \lambda) + \Phi_{\beta_R}] \\ &\approx -(0.511 + 0.06775\alpha + 0.00917\alpha^4 + 0.00117\alpha^6)\kappa_c\alpha, \end{aligned} \tag{4.16}$$

where α is in radian. The cross-flow velocity along the mantle permits a constant supply of mass transport, or spillage as it were, from the outer, annular stream to the core region. Both $(u_\phi)_{max}/\sigma_c$ and ϕ_{max}, including the approximate expression given by (4.14), are illustrated in figure 7(*a*). The cross-flow velocities, rendered in both

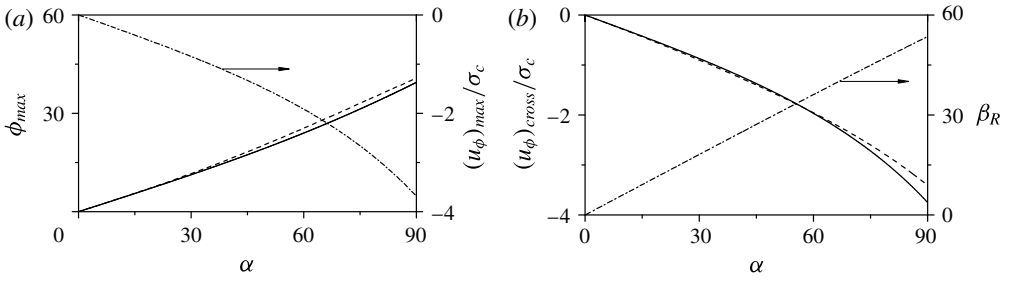

FIGURE 7. Variation with α of (*a*) ϕ_{max} (——), $\tilde{\phi}_{max}$ (– – –) and $(u_\phi)_{max}$ (— · —); (*b*) $(u_\phi)_{cross}$ (——), $(\tilde{u}_\phi)_{cross}$ (– – –) and $\phi_{cross} = \beta_R$ (— · —).

exact and approximate forms by (4.16), are displayed side by side in figure 7(*b*) along with the mantle loci along which flow crossing occurs. It may be seen that $(u_\phi)_{max}$ mirrors the cross-flow velocity so closely that the two profiles appear to be nearly indistinguishable. This behaviour is interesting because each of these velocities stands at a different angle.

4.6. *Pressure distribution*

The pressure may be directly evaluated from Euler's momentum equation. The partial derivatives of the pressure for both cylindrical and spherical coordinates return

$$\frac{\partial p}{\partial r} = \frac{1}{r^3\sqrt{1+\zeta^2}} + \frac{\kappa_c^2}{r\sqrt{1+\zeta^2}}\left[\zeta^2\sqrt{1+\zeta^2} - \zeta^3 + \zeta(1+\zeta^2)^{-1/2}(\lambda - \ln Z - 1)\right] \quad (4.17)$$

and

$$\frac{\partial p}{\partial z} = \frac{\kappa_c^2}{r\sqrt{1+\zeta^2}}\left(\zeta^2 - \zeta\sqrt{1+\zeta^2} - \lambda + \ln Z + 1\right). \quad (4.18)$$

Taking the normalized p_0 as our baseline at the inlet of the cone where $(r, z) = (1, \cot\alpha)$, then (4.17) and (4.18) may be partially integrated to yield, $\Delta p(\alpha) = p(\alpha) - p_0(\alpha)$, where p_0 may be correlated to the cone geometry as shown in table 2. One deduces

$$p(r, z) = -\frac{1}{2r^2} + \frac{1}{2}\kappa_c^2[(\zeta + \zeta^3)(1+\zeta^2)^{-1/2} - \zeta^2 - \ln^2 Z - (2\lambda - 1)\ln(Z + 2\zeta)]. \quad (4.19)$$

Figure 8 illustrates the behaviour of Δp at several axial stations and $\sigma_c = 1$. It is clear that the pressure variation is dominated by its $(-r^{-2}/2)$ leading-order term, a result that is equally shared by the bidirectional vortex solution in a straight cylinder. It is also characteristic of other cyclonic studies such as those by Pervov (1974), Mikhaylov & Romenskiy (1974), Pericleous (1987), Zhou & Soo (1990), Concha (2007), Cortes & Gil (2007) and Hoffmann & Stein (2008). In both cylindrical and conical configurations, the pressure difference is largest near the centreline and negligible near the side wall.

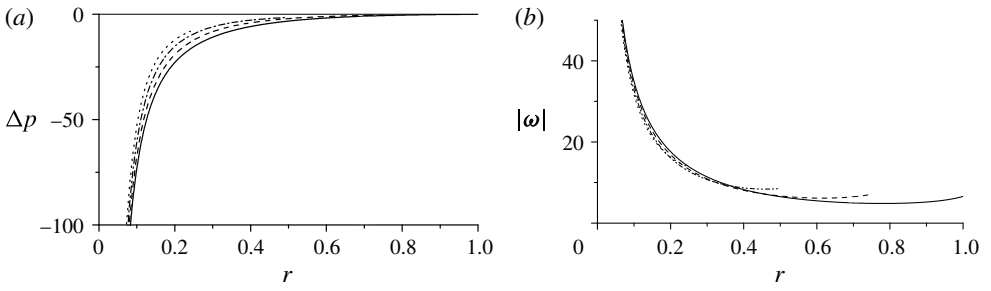

FIGURE 8. Radial distribution of (*a*) pressure referenced to the apex and (*b*) total vorticity at several axial positions and $\alpha = 45°$.

α	5°	10°	15°	20°	25°	30°	35°	40°	45°
p_0	50.32	31.15	22.04	16.49	12.68	9.88	7.73	6.02	4.63
α	50°	55°	60°	65°	70°	75°	80°	85°	90°
p_0	3.48	2.53	1.73	1.07	0.522	0.091	−0.226	−0.429	−0.500

TABLE 2. Pressure constant p_0 versus α for $\sigma_c = 1$.

4.7. *Vorticity distribution*

Finally, the vorticity may be straightforwardly evaluated using $\boldsymbol{\omega} = \boldsymbol{\nabla} \times \boldsymbol{u}$ to show that a special relation exists between $\boldsymbol{u}$ and $\boldsymbol{\omega}$. We find

$$\boldsymbol{u} = \frac{B(\psi)}{\kappa_c}\boldsymbol{\omega} = \frac{\sqrt{1 + 2\kappa_c \psi}}{\kappa_c}\boldsymbol{\omega}. \tag{4.20}$$

The vector parallelism reflected by (4.20) helps to confirm that the reconstructed Bloor–Ingham solution belongs to the category of helical motions known as 'Beltrami' or 'Beltramian' (see Wu, Ma & Zhou 2006).

In closing, the radial variation of the total vorticity is displayed in figure 8(*b*) at several fixed locations. The vorticity lines confirm the duality of radial positions that yield the same value of ω at fixed z. This behaviour may be attributed to the transport of vorticity along looping streamlines. It is further explored in figure 9 where isovorticity lines are shown for a conical cyclone with divergence half-angles of 30° and 45°. The resulting vorticity maps confirm the transport of vorticity along mean flow streamlines. As for the magnitude of vorticity, it increases as the axis of rotation is approached, especially inside an approximately 20 % radius. The region in question is labelled 'high intensity core vorticity' in figure 9. Here too, the over-amplification at the origin is caused by the absence of viscous damping.

5. Conclusions

This article revisits the problem arising in the context of a bidirectional vortex in a conical chamber. Immediate applications include industrial cyclone separators and modified forms of the swirl-driven liquid and hybrid rocket engines. Starting with the spherical Bragg–Hawthorne equation, an exact Euler solution is derived that overcomes some of the limitations of previous models of conical cyclones. Our results are presented in both spherical and polar cylindrical coordinates to facilitate

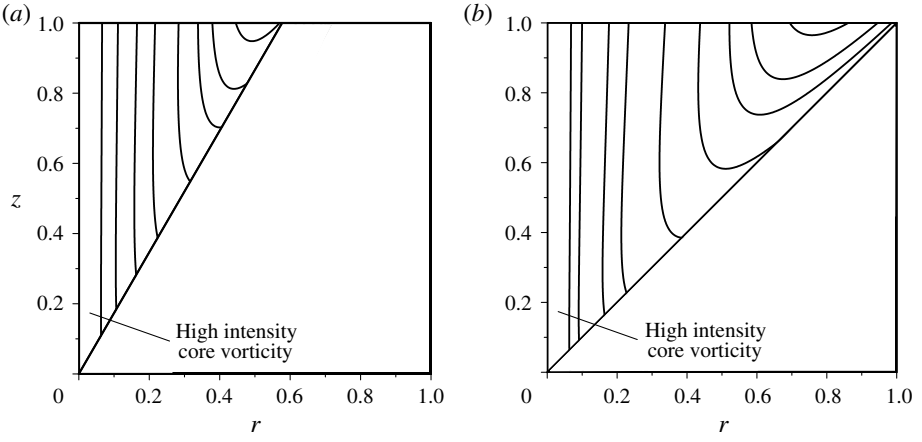

FIGURE 9. Isovorticity lines for (*a*) $\alpha = 30°$ and (*b*) 45°.

cross-referencing. Through a judicious choice of normalizing parameters, a universal, self-similar Beltramian formulation is obtained independently of the cone's vertical dimension. The ensuing analysis enables us to identify important parameters such as:

(i) the closed-form pressure and vorticity distributions;
(ii) the spatially invariant ratio between the velocity and vorticity vectors;
(iii) the mantle inclination at 60 % of the cone's divergence half-angle;
(iv) the cross-flow velocity along the mantle interface $(u_\phi)_{cross}$;
(v) the conical swirl number σ_c; and
(vi) the maximum zenith velocity $|u_\phi|$ and its locus ϕ_{max}.

The latter is reminiscent of the radial velocity in a right-cylindrical chamber. It is interesting that our theoretical prediction for β is fully corroborated by the experimental measurements of Bradley & Pulling (1959). Our analysis also confirms that the cyclonic motion in question is of the Beltramian type, which is consistent with the findings of Majdalani (2012), where a similar class of Beltramian and Trkalian flows is identified in the context of a right-cylindrical chamber.

After expressing the streamfunction in polar cylindrical form, $\psi = \kappa_c r^2(\lambda - \ln Z - Z\sqrt{1+\zeta^2})/2$, this work enables us to deduce the fundamental expression linking the tangential angular momentum and the streamfunction through $B = ru_\theta = \sqrt{1+2\kappa_c\psi}$. This relation plays a central role in the Bragg–Hawthorne formulation as it leads to a solution that is capable of satisfying the problem's basic constraints in a frictionless environment. It thus complements previous studies such as those by Bloor & Ingham (1987) and Majdalani & Rienstra (2007). In hindsight, its primitive form could have been posited at the beginning of the analysis to precipitate the solution more expeditiously. Similar forms of B may be employed while seeking other solutions to this class of helical flows. These include $B = B_0$, $\sqrt{B_0 + B_1\psi}$, $\sqrt{B_0 + B_1\psi^{\pm m}}$, $B_0\psi$, $B_0\psi^{\pm m}$, ..., and others. Along similar lines, a generalization beyond $H = \text{const.}$ may be attempted in the quest for more elaborate flow profiles.

Acknowledgements

This work was supported partly by the National Science Foundation and partly by the Hugh and Loeda Francis Chair of Excellence, Department of Aerospace Engineering, Samuel Ginn College of Engineering, Auburn University. T.A.B. was a Research Associate of J.M. at the time this work was undertaken.

Appendix A. Conical swirl number

Through the use of (2.8), the inlet axial velocity W may be eliminated in favour of the actual tangential flow rate into the chamber,

$$W = \frac{\bar{Q}_i}{\pi(b^2 - a^2)} = -\frac{UA_i}{\pi a^2(1 - X_\beta^2)}, \tag{A 1}$$

where $X_\beta = b/a$. For consistency with the bidirectional vortex study of Vyas & Majdalani (2006), the swirl parameter may be written as

$$S = \frac{\pi ab}{A_i} = \frac{\pi X_\beta}{Q_i} = \pi X_\beta \sigma, \tag{A 2}$$

where $\sigma = Ua^2 Q_i^{-1} = a^2/A_i$ is the modified swirl number. The conventional swirl parameter, S, corresponds to the form used by Hoekstra *et al.* (1999) and Derksen & van den Akker (2000). Accordingly, we have

$$W = -\frac{U}{\pi\sigma(1 - X_\beta^2)} = -\frac{U}{\pi\sigma_c}. \tag{A 3}$$

Following Majdalani & Rienstra (2007), a modified swirl parameter appropriate of conical cyclones may be defined as

$$\sigma_c = \frac{a^2 - b^2}{A_i} = \frac{L^2}{A_i}(\tan^2\alpha - \tan^2\beta) = \frac{a^2}{A_i} l^2(\tan^2\alpha - \tan^2\beta) = \sigma\left(1 - \frac{\tan^2\beta}{\tan^2\alpha}\right), \tag{A 4}$$

where $\beta = \tan^{-1}(b/L)$ is the angle of the mantle throughout the cone. It may be easily verified that σ_c equates to the tangential-to-axial velocity ratio and that σ_c is related to σ via

$$\sigma_c = \sigma(1 - X_\beta^2) = -\frac{U}{\pi W}, \tag{A 5}$$

where the negative sign is simply transferred to the Bragg–Hawthorne equation.

Appendix B. Partial solution of the Bragg–Hawthorne equation

B.1. *Streamfunction representation*

Inserting the product solution into (3.11) gives rise to a second-order ordinary differential equation, specifically,

$$2G + \sin\phi \frac{\mathrm{d}}{\mathrm{d}\phi}\left(\frac{1}{\sin\phi}\frac{\mathrm{d}G}{\mathrm{d}\phi}\right) = -\kappa_c. \tag{B 1}$$

The solution to (B 1) may be retrieved by setting the two complementary and particular solutions as

$$G_1 = \sin^2\phi; \quad G_2 = g(\phi)\sin^2\phi; \quad G_p = -\tfrac{1}{2}\kappa_c. \tag{B 2a–c}$$

Backward substitution into (B 1) yields

$$g(\phi) = -\tfrac{1}{2}[\csc\phi\cot\phi + \ln(\csc\phi + \cot\phi)] \tag{B 3}$$

and so

$$G = -\tfrac{1}{2}\kappa_c + K_1\sin^2\phi + K_2[\cos\phi - (\sin^2\phi)\ln\Phi]. \tag{B 4}$$

As usual, we fix the streamfunction at both the axis of symmetry and the conical wall. Using $\psi(R,0) = \psi(R,\alpha) = 0$, we deduce $G(0) = G(\alpha) = 0$ and so both K_1 and K_2 may be written as

$$K_1 = \tfrac{1}{2}\kappa_c(\csc^2\alpha - \cot\alpha\csc\alpha + \ln\mathcal{A}); \quad K_2 = \tfrac{1}{2}\kappa_c, \tag{B 5a,b}$$

which enables us to fold (B 4) into

$$G = \frac{\kappa_c\sin^2\phi}{2}(\lambda - \ln\Phi + \csc\phi\cot\phi - \csc^2\phi), \tag{B 6}$$

which is the precursor to (3.12).

B.2. *Velocities*

With the streamfunction at hand, u_R and u_ϕ may be readily determined. Through proper differentiation, we obtain (3.15) and (3.16). To produce the tangential velocity, we use (3.10) and solve for B. Straightforward integration renders

$$\int B\,\mathrm{d}B = \int \kappa_c\,\mathrm{d}\psi \quad \text{or} \quad B(\psi) = \sqrt{2\kappa_c\psi + B_0}. \tag{B 7a,b}$$

At the inlet, $\psi = (R^2\sin^2\phi - 1)/(2\kappa_c)$, which, when substituted into (B 7), returns $B_0 = 1$, and so

$$B(\psi) = \sqrt{1 + 2\kappa_c\psi}. \tag{B 8}$$

It may be helpful to clarify that the previous inlet streamfunction is evaluated here at the top of the cone, namely, at the wall where $\psi = (R^2\sin^2\phi - 1) = 0$ and where $B = 1$. Next, we may update (B 8) into

$$u_\theta = \frac{1}{R\sin\phi}\sqrt{1 + 2\kappa_c\psi}. \tag{B 9}$$

Note that we recover (3.8) along the inlet section, where a uniform flow prevails. Finally, using the streamfunction inside the cone, we retrieve (3.17).

B.3. *Spherical to cylindrical transformation*

In order to obtain (3.19), our expressions are switched from spherical to polar cylindrical coordinates using the standard transformation matrix,

$$\left.\begin{aligned} u_r &= u_R\sin\phi + u_\phi\cos\phi, \\ u_z &= u_R\cos\phi - u_\phi\sin\phi. \end{aligned}\right\} \tag{B 10}$$

REFERENCES

ALEXANDER, R. M. 1949 Fundamentals of cyclone design and operation. In *Proceedings of the Australasian Institute of Mining and Metallurgy*, pp. 203–228; N.S., Nos., 152–153. Australasian Institute of Mining and Metallurgy.

AVCI, A. & KARAGOZ, I. 2003 Effects of flow and geometrical parameters on the collection efficiency in cyclone separators. *J. Aero. Sci.* **34** (7), 937–955.

BARTH, W. 1956 Berechnung und Auslegung von Zyklonabscheidern aufgrund neuerer Untersuchungen (Design and layout of the cyclone separator on the basis of new investigations). *Brennstoff-Warme-Kraft* **8** (1), 1–9.

BLOOR, M. I. G. & INGHAM, D. B. 1973 Theoretical investigation of the flow in a conical hydrocyclone. *Trans. Inst. Chem. Engrs* **51** (1), 36–41.

BLOOR, M. I. G. & INGHAM, D. B. 1987 The flow in industrial cyclones. *J. Fluid Mech.* **178**, 507–519.

BOYSAN, F., AYERS, W. H. & SWITHENBANK, J. 1982 A fundamental mathematical modelling approach to cyclone design. *Chem. Engng Res. Des.* **60**, 222–230.

BRADLEY, D. 1965 *The Hydrocyclone*. Pergamon.

BRADLEY, D. & PULLING, D. J. 1959 Flow patterns in the hydraulic cyclone and their interpretation in terms of performance. *Trans. Inst. Chem. Engrs* **37**, 34–45.

BRAGG, S. L. & HAWTHORNE, W. R. 1950 Some exact solutions of the flow through annular cascade actuator disks. *J. Aero. Sci.* **17** (4), 243–249.

CHESNOKOV, YU. G., BAUMAN, A. V. & FLISYUK, O. M. 2006 Calculation of the velocity field of a fluid in a hydrocyclone. *Russian J. Appl. Chem.* **79** (5), 774–777.

CHIAVERINI, M. J., MALECKI, M. J., SAUER, J. A., KNUTH, W. H. & MAJDALANI, J. 2003 Vortex thrust chamber testing and analysis for O2-H2 propulsion applications. In *39th AIAA/ASME/SAE/ASEE Joint Propulsion Conference and Exhibit, Huntsville, AL. AIAA Paper* 2003-4473.

CHU, L.-Y. & CHEN, W.-M. 1993 Research on the motion of solid particles in a hydrocyclone. *Separation Sci. Technol.* **28** (10), 1875–1886.

CONCHA, F. 2007 Flow pattern in hydrocyclones. *Kona-Powder Particle* **25**, 97–132.

CONCHA, F., BARRIENTOS, A., MUNOZ, L., BUSTAMANTE, O. & CASTRO, O. 1996 A phenomenological model of a hydrocyclone. In *International Conference on Hydrocyclones '96* (ed. D. Claxton, L. Svarovsky & M. T. Thew), pp. 63–82. MEP Ltd.

CORTES, C. & GIL, A. 2007 Modeling the gas and particle flow inside cyclone separators. *Prog. Energy Combust. Sci.* **33** (5), 409–452.

DABIR, B. & PETTY, C. A. 1986 Measurements of mean velocity profiles in a hydrocyclone using laser doppler anemometry. *Chem. Engng Commun.* **48** (4), 377–388.

DERKSEN, J. J. 2003 Separation performance predictions of a Stairmand high-efficiency cyclone. *Fluid Mech. Transp. Phenom.* **49**, 1359–1371.

DERKSEN, J. J. & VAN DEN AKKER, H. E. A. 2000 Simulation of vortex core precession in a reverse-flow cyclone. *AIChE J.* **46** (7), 1317–1331.

DERKSEN, J. J., VAN DEN AKKER, H. E. A. & SUNDARESAN, S. 2008 Two-way coupled large-eddy simulations of the gas–solid flow in cyclone separators. *AIChE J.* **54** (4), 872–885.

DIETZ, P. W. 1981 Collection efficiency of cyclone separators. *AIChE J.* **27** (6), 888–892.

ESCUDIER, M. P. 1987 Confined vortices in flow machinery. *Annu. Rev. Fluid Mech.* **19**, 27–52.

FANG, D., MAJDALANI, J. & CHIAVERINI, M. J. 2003 Simulation of the cold-wall swirl driven combustion chamber. In *39th AIAA/ASME/SAE/ASEE Joint Propulsion Conference and Exhibit, Huntsville, AL. AIAA Paper* 2003-5055.

FONTEIN, F. J. & DIJKSMAN, C. 1953 *Recent Developments in Mineral Dressing*. Institution of Mining and Metallurgy.

HARVEY, J. K. 1962 Some observations of the vortex breakdown phenomenon. *J. Fluid Mech.* **14**, 585–592.

HOEKSTRA, A. J., DERKSEN, J. J. & VAN DEN AKKER, H. E. A. 1999 An experimental and numerical study of turbulent swirling flow in gas cyclones. *Chem. Engng Sci.* **54** (13), 2055–2065.

HOFFMANN, A. C. & STEIN, L. E. 2008 *Gas Cyclones and Swirl Tubes*, 2nd edn. Springer.

HSIEH, K. T. & RAJAMANI, R. K. 1988 Phenomenological model of the hydrocyclone: model development and verification for single-phase flow. *Intl J. Miner. Process.* **22** (1–4), 223–237.

HSIEH, K. T. & RAJAMANI, R. K. 1991 Mathematical model of the hydrocyclone based on physics of fluid flow. *AIChE J.* **37** (5), 735–746.

HU, L. Y., ZHOU, L. X., ZHANG, J. & SHI, M. X. 2005 Studies of strongly swirling flows in the full space of a volute cyclone separator. *AIChE J.* **51** (3), 740–749.

IOZIA, D. L. & LEITH, D. 1989 Effect of cyclone dimensions on gas flow pattern and collection efficiency. *Aerosol Sci. Technol.* **10** (3), 491–500.

KELSALL, D. F. 1952 A study of the motion of solid particles in a hydraulic cyclone. *Trans. Inst. Chem. Engrs* **30**, 87–103.

KELSALL, D. F. 1953 A further study of the hydraulic cyclone. *Chem. Engng Sci.* **2** (6), 254–272.

KNOWLES, S. R., WOODS, D. R. & FEUERSTEIN, I. A. 1973 The velocity distribution within a hydrocyclone operating without an air core. *Can. J. Chem. Engng* **51** (3), 263–271.

KNUTH, W. H., BEMOWSKI, P. A., GRAMER, D. J., MAJDALANI, J. & ROTHBAUER, W. J. 1996 Gas-fed, vortex injection hybrid rocket engine. SBIR Phase I, NASA Final Technical Contract no. *NAS* 8-40679. Orbital Technologies Corporation, Madison, Wisconsin.

KNUTH, W. H., CHIAVERINI, M. J., SAUER, J. A. & GRAMER, D. J. 2002 Solid-fuel regression rate behavior of vortex hybrid rocket engines. *J. Propul. Power* **18** (3), 600–609.

LEIBOVICH, S. 1978 The structure of vortex breakdown. *Annu. Rev. Fluid Mech.* **10**, 221–246.

LEIBOVICH, S. 1984 Vortex stability and breakdown: survey and extension. *AIAA J.* **22** (9), 1192–1206.

LEITH, D. & LICHT, W. 1972 The collection efficiency of cyclone type particle collectors – a new theoretical approach. *AIChE Symposium Series* **68** (126), 196–206.

LEITH, D. & MEHTA, D. 1973 Cyclone performance and design. *Atmos. Environ.* **7** (5), 527–549.

LI, P. M., LIN, S. & VATISTAS, G. H. 1987 Predicting collection efficiency of separation cyclones: a momentum analysis. *Can. J. Chem. Engng* **65** (5), 730–735.

TER LINDEN, A. J. 1949 Investigations into cyclone dust collectors. *Proc. Inst. Mech. Engrs* **160**, 233–251.

LUO, Q. A., DENG, C. L., XU, J. R., YU, L. X. & XIONG, G. G. 1989 Comparison of the performance of water-sealed and commercial hydrocyclones. *Intl J. Miner. Process.* **25** (3–4), 297–310.

MAJDALANI, J. 2007 *Vortex Injection Hybrid Rockets*, chap. 6, pp. 247–276. AIAA Progress in Astronautics and Aeronautics.

MAJDALANI, J. 2012 Helical solutions of the bidirectional vortex in a cylindrical cyclone: Beltramian and Trkalian motions. *Fluid Dyn. Res.* **44** (6), 065506.

MAJDALANI, J. & CHIAVERINI, M. J. 2017 Characterization of GO2-GH2 simulations of a miniature vortex combustion cold wall chamber. *J. Propul. Power* **33** (2), 387–397.

MAJDALANI, J. & RIENSTRA, S. W. 2007 On the bidirectional vortex and other similarity solutions in spherical coordinates. *Z. Angew. Math. Mech.* **58** (2), 289–308.

MIKHAYLOV, P. M. & ROMENSKIY, A. A. 1974 On calculation of flow dynamics in liquid cyclones. *Fluid Mech. – Sov. Res.* **3** (1), 154–159.

MONREDON, T. C., HSIEH, K. T. & RAJAMANI, R. K. 1992 Fluid flow model of the hydrocyclone: an investigation of device dimensions. *Intl J. Miner. Process.* **35** (1–2), 65–83.

MOTHES, H. & LÖFFLER, F. 1985 Motion and deposition of particles in cyclones. *German Chem. Enging* **8** (4), 223–233.

PENG, W., HOFFMANN, A. C., BOOT, P. J. A. J., UDDING, A., DRIES, H. W. A., EKKER, A. & KATER, J. 2002 Flow pattern in reverse-flow centrifugal separators. *Powder Technol.* **127** (3), 212–222.

PENG, W., HOFFMANN, A. C. & DRIES, H. 2004 Separation characteristics of swirl-tube dust separators. *AIChE J.* **50** (1), 87–96.

PERICLEOUS, K. A. 1987 Mathematical simulation of hydrocyclones. *Appl. Math. Model.* **11** (4), 242–255.

PERVOV, A. A. 1974 Investigation of velocity and pressure zones in SDK-TsN-33 and SK-TsN-34 cyclones. *Chem. Petroleum Engng* **10** (10), 898–900.

ROM, C. J. 2006 Flow field and near nozzle fuel spray characterizations for a cold flowing vortex engine. MS thesis, University of Wisconsin, Madison, Department of Engineering Mechanics and Engineering Physics.

ROM, C. J., ANDERSON, M. H. & CHIAVERINI, M. J. 2004 Cold flow analysis of a vortex chamber engine for gelled propellant combustor applications. In *40th AIAA/ASME/SAE/ASEE Joint Propulsion Conference and Exhibit, Fort Lauderdale, FL. AIAA Paper* 2004-3359.

SAUER, J. A., KNUTH, W. H., MALECKI, M. J., CHIAVERINI, M. J. & HALL, C. D. 2002 Development of a LOX/RP-1 vortex combustion cold-wall thrust chamber assembly. In *38th AIAA/ASME/SAE/ASEE Joint Propulsion Conference and Exhibit, Indianapolis, IN. AIAA Paper* 2002-4144.

SHEPHERD, C. B. & LAPPLE, C. E. 1939 Flow pattern and pressure drop in cyclone dust collectors. *Ind. Engng Chem.* **31** (8), 972–984.

SHEPHERD, C. B. & LAPPLE, C. E. 1940 Flow pattern and pressure drop in cyclone dust collectors: cyclone without inlet vane. *Ind. Engng Chem.* **32** (9), 1246–1248.

SMITH, J. L. 1962*a* An analysis of the vortex flow in the cyclone separator. *Trans. ASME J. Basic Engng* **84D** (4), 609–618.

SMITH, J. L. 1962*b* An experimental study of the vortex in the cyclone separator. *Trans ASME J. Basic Engng* **84** (4), 602–608.

STAIRMAND, C. J. 1951 The design and performance of cyclone separators. *Trans. Inst. Chem. Engrs* **29**, 356–383.

VYAS, A. B. & MAJDALANI, J. 2006 Exact solution of the bidirectional vortex. *AIAA J.* **44** (10), 2208–2216.

WU, J.-Z., MA, H.-Y. & ZHOU, M.-D. 2006 *Vorticity and Vortex Dynamics*. Springer.

XIANG, R., PARK, S. H. & LEE, K. W. 2001 Effects of cone dimension on cyclone performance. *J. Aero. Sci.* **32** (4), 549–561.

ZHOU, L. X. & SOO, S. L. 1990 Gas–solid flow and collection of solids in a cyclone separator. *Powder Technol.* **63** (1), 45–53.